Computers and Concrete, *Vol. 18, No. 3 (2016) 319-336*
DOI: http://dx.doi.org/10.12989/cac.2016.18.3.319

Numerical analysis of the thermal behaviors of cellular concrete

Wei She*[1,3,4], Guotang Zhao[2], Guotao Yang[2], Jinyang Jiang[1], Xiaoyu Cao[1]
and Yi Du[1]

[1]*Jiangsu Key laboratory for Construction Materials, Southeast University, Nanjing, 211189, P.R. China*
[2]*China Railway Corporation, Beijing 100844, China*
[3]*Jiangsu Institute of Building Science Co. LTD, Nanjing 210008, P. R. China*
[4]*Concrete Technology Unit, Division of Civil Engineering, University of Dundee, Dundee DD1 4HN, Scotland, UK*

(Received March 23, 2015, Revised April 17, 2016, Accepted May 17, 2016)

Abstract. In this study, both two- and three-dimensional (2D and 3D) finite-volume-based models were developed to analyze the heat transfer mechanisms through the porous structures of cellular concretes under steady-state heat transfer conditions and to investigate the differences between the 2D and 3D modeling results. The 2D and 3D reconstructed pore networks were generated from the microstructural information measured by 3D images captured by X-ray computerized tomography (X-CT). The computed effective thermal conductivities based on the 2D and 3D calculations performed on the reconstructed porous structures were found to be nearly identical to those evaluated from the 2D cross-sectional images and the 3D X-CT images, respectively. In addition, the 3D computed effective thermal conductivity was found to agree better with the measured values, in comparison with the 2D reconstruction and real cross-sectional images. Finally, the thermal conductivities computed for different reconstructed porous 3D structures of cellular concretes were compared with those obtained from 2D computations performed on 2D reconstructed structures. This comparison revealed the differences between 2D and 3D image-based modeling. A correlation was thus derived between the results of the 3D and 2D models.

Keywords: Finite volume method (FVM); Effective thermal conductivity (ETC); image-based modeling; cellular concrete; Guarded hot-plate method (GHP)

1. Introduction

Cellular concrete is a type of lightweight concrete. These materials are generally lightweight, sound-proof, thermally insulating and resistant to failures caused by insect, bacterial and fire damages (Scheffler and Paolo 2005).Cellular concretes entrap air-voids in the cement paste or mortar matrix by using a suitable foaming agent and are classified into two groups based on the method of pore structure formation (Tanacan *et al.* 2009): the air-entraining method (aerated concrete uses chemical reactions in the paste to produce gas, e.g., aluminum powder and H_2O_2)

---

*Corresponding author, Ph.D., E-mail: weishe@aliyun.com

Copyright © 2016 Techno-Press, Ltd.
http://www.techno-press.org/?journal=cac&subpage=8 ISSN: 1598-8198 (Print), 1598-818X (Online)

and the foaming method (foamed concrete introduces air into the paste with pre-foamed foam). Based on the curing conditions, cellular concrete can also be divided into two groups: one consists of masonry products that are autoclaved at a temperature higher than 100 °C in a pressurized and steam-heated environment (autoclave aerated concrete, AAC) and the other is cured at ambient or slightly elevated temperatures (Non-AAC).

In recent years, builders around the world have become increasingly interested in using cellular concrete. This interest comes from the decreased dosage of load-bearing elements, and the superior thermal properties of cellular concrete compared with conventional concrete. Regarding the thermal properties, dry densities of 300-500kg/m^3 are usually utilized. No strict strength characteristics are required, therefore, the thermal performance of lightweight concrete commonly plays the more dominant role (Aldridge 2000, Jones and McCarthy 2005, Kearsley and Mostert 2005, Narayanan and Ramamurthy 2000, Esmaily and Nuranian 2012). Therefore, the accurate determination of the effective thermal conductivity, k_e, is essential in engineering applications. For porous materials with two phases (solid and fluid), thermal properties primarily depend on the thermal performance of the constituent materials (i.e., the ratio of the thermal conductivities of the solid and fluid phases) and the microstructure (the spatial distribution of the phases and the contact thermal resistance between non-consolidated particles (Placido *et al*. 2005, Glicksman 1994, Kuhn *et al*. 1992)). Furthermore, cellular concrete can be designed to satisfy the construction requirements by varying material parameters such as the cement paste composition, bubble size and volume friction. Therefore, an accurate evaluation of the relationship between the microstructure and the thermal transfer properties of these porous lightweight building materials is required.

Determining of the relationship between the microstructure and effective thermal property of porous materials can be accomplished either experimentally (Mydin and Wang 2012, Mohdzahari *et al*. 2009) or analytically by assuming simplified geometries (Wiener *et al*. 1904, Hashin and Shtrikman 1962, Landauer 1952, Russell 1935, Glicksmann 1994, Bhattacharya *et al*. 2002). The former approach is expensive and time consuming, and the validity of the results is usually limited to the experimental conditions. The latter approach is limited by the validity of the underlying simple assumptions for the complex geometry. However, several of these limitations can be overcome by the combined experimental-numerical technique presented in this paper.

This study developed 2D and 3D image-based finite volume models to analyze the heat transfer mechanisms through the porous structure of cellular concrete under steady-state condition. The microstructure of cellular concrete was quantitatively characterized by a three-dimensional X-ray computerized tomography technology (3D-XCT) considering only the gas and solid phases. The 2D and 3D images were then reconstructed by a random generation method that retained the essential microstructural features. These real and reconstructed images (2D and 3D) were used to estimate the thermal conductivities of cellular concretes using a finite volume numerical method (FVM). The numerical results were also validated through a comparison with experimental results. Finally, comparisons of the effective thermal conductivities obtained from the reconstructed 3D image and reconstructed 2D images revealed a relationship between the 2D and 3Dmodeling.

2. Thermal conductivity measurements

The experimental apparatus used in this study was a guarded hot-plate that was designed based on the standards required for steady-state measurements (ISO 8990 1994, EN 12939 2000, EN

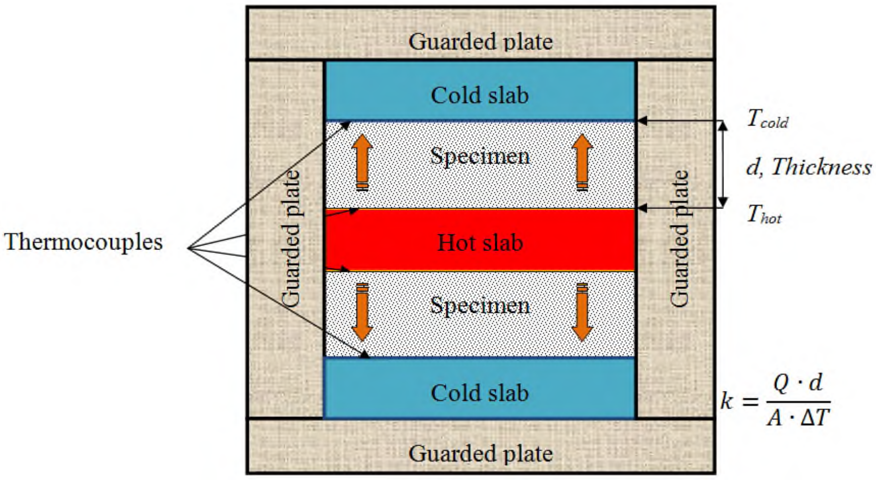

Fig. 1 Experimental apparatus. The guarded hot-plate method establishes a one-dimensional heat flow through a pair of specimens. The guarded plate was made of expanded polystyrene (EPS)

12664 2001). The guarded hot-plate method (GHP) (see Fig. 1) established a one-dimensional heat flow through a pair of specimens by reducing the undesired lateral heat flows to negligible proportions (Zarr 2001, Yesilata and Turgut 2007). The apparatus presented here was adapted from the one used to measure the U-value of a wall according to the standard required for steady-state measurements (ISO 8990 1994).

Our system could test materials with a thickness rangingfrom10 mm to 100mm. Fig.1 shows the collocation of specimens between the hot and cold slabs. Heat was electrically supplied at a known rate to the hot-slab. A constant temperature difference between the hot and cold slabs was maintained. The temperature differences were controlled through thermocouples on the surfaces of the slabs. The energy consumed was registered using an external wattmeter that analyzed and transmitted the data to a computer. The temperature was continuously measured and controlled with a Proportional-Integral-Derivative (PID) regulator to maintain the required temperature gradient. The guarded plates acted as thermal barriers to secure the one dimensional heat flow from the main heater to the cold plate. This one-directional heat flow enables the exact measurement of the Q value.

In our experiments, the specimens, the cold slab, and the hot slab are initially at identical temperatures (313.5 K). At the beginning of the experiment, the temperature of the cold plate is lowered from 313.5 K to 273.5 K. The humidity of the room was controlled and maintained below 50%. The box was placed in a hot chamber operating at a fixed temperature, humidity and air flow. Temperature and relative humidity sensors are positioned at several points to measure the corresponding air conditions.

After 28 days of sealed curing, specimens of cellular concrete (300mm×300mm×30mm) were oven dried at a temperature of 80°C until a constant mass was observed (approximately four days). Samples were dried to eliminate any moisture that was retained in the slabs, because the moisture would affect the conductivity results (Mydin and Wang 2012). The oven temperature was below the boiling point to avoid sample cracking (Wang *et al*. 2005). The high speed of water evaporation and the thermal mismatch between the compositions will create a more connected path and cracks for the heat to flow through. This process will reduce the reliability of thermal testing.

Heat was allowed to flow between the two plates until the system stabilized. The maximum time allowed for the samples to stabilize was about three hours. The thermal conductivity based on the GHP method can then be calculated using the Fourier heat flow equation

$$k = \frac{Q \cdot d}{C \cdot \Delta T} \tag{1}$$

Where k is the effective thermal conductivity of the tested sample; Q is the time rate of heat flow; d is the thickness of the tested sample; and C and ΔT are the cross-sectional area and temperature difference across the sample, respectively. This test method is useful for generating thermal data on deformable flexible specimens and has been considered as a primary technique for precise thermal conductivity measurements. The uncertainty of the thermal conductivity measurements considering both random and systematic errors was evaluated to be 2% with a confidence level of 95%.

3. Finite volume numerical model

The implementation of a finite-volume method to estimate the effective thermal conductivity of porous concrete was first proposed by (Wei *et al.* 2013). The method is based on the analysis of the temperature distribution in the microstructure of the foam by considering the governing differential equation for the steady-state heat conduction without internal heat generation. The model simulated the steady-state thermal conductivity experimental apparatus. The modeled structure is a slab of porous material with perfectly insulated sides which is sandwiched between two slabs of non-porous solid material maintained at temperatures T_{hot} and T_{cold} (see Fig. 2). The steady-state heat conduction equation expresses the heat balance at each point of the two-phase porous material.

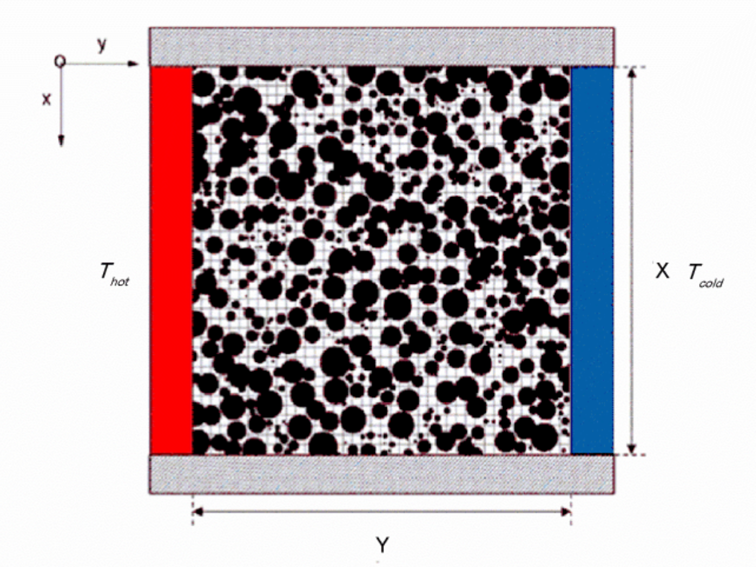

Fig. 2 2-D illustration of the ETC computation

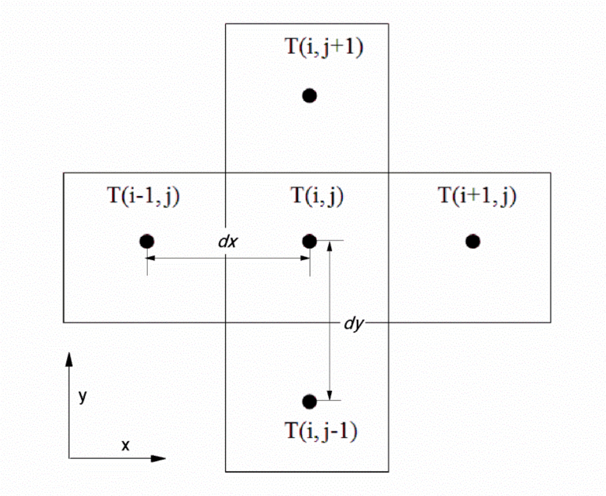

Fig. 3 Schematic view of a cell in the 2D model, including the four neighbors of the cell

Additionally, the conduction through the solid phase, conduction through the gas phase, convection of the gas and radiation are generally the primary mechanisms contributing to the thermal conductivity of a cellular material(Gibson and Ashby 1997).Considering the previous studies by Skochdopole (1961) and Lu and Chen (1999),the heat transfer by convection can be negligible for void diameters smaller than 4 mm, and the experimental temperature for ETC is not substantially high. Therefore, only the conduction mechanisms in two phases are considered in this study.

3.1 2D numerical model

In the two dimensional model, the steady thermal transfer equation can be expressed as the following

$$\frac{\partial}{\partial x}\left(\lambda_{i,j}\frac{\partial T}{\partial x}\right)+\frac{\partial}{\partial y}\left(\lambda_{i,j}\frac{\partial T}{\partial y}\right)=0 \tag{2}$$

where $\lambda_{i,j}$ is the thermal conductivity and T is the temperature. With regards to a five-point integration formula, a schematic view of a cell of the domain (i.e., a pixel of the binary image) and its four neighbors is presented in Fig. 3. For square pixels, the above equation can be discretized as follows

$$\begin{aligned}&-(T(i+1,j)-T(i,j))\cdot\lambda(i+1/2,j)\\&+(T(i,j)-T(i-1,j))\cdot\lambda(i-1/2,j)\\&-(T(i,j+1)-T(i,j))\cdot\lambda(i,j+1/2)\\&+(T(i,j)-T(i,j-1))\cdot\lambda(i,j-1/2)=0\end{aligned} \tag{3}$$

where$\lambda_{(i+1/2,\,j)}$ represents the thermal conductivity between cell center (i,j) and (i +1,j) . These terms can be expressed as the following

$$\lambda(i+1/2, j) = 2/(\frac{1}{\lambda(i, j)} + \frac{1}{\lambda(i+1, j)}) \tag{4}$$

The thermal conductivity *λ(i,j)* is assigned to each pixel depending on the corresponding material (e.g., cement paste for the white pixels and pores for the black pixels). For the considered images, the boundary conditions are set by applying a constant temperature on the left side edge (313.5K) as well as on the right side (273.5K), and a zero flux is applied for the other two edges (i.e., top and bottom). The corresponding mathematical expression is as follows

$$\left.\frac{\partial T}{\partial x}\right|_{x=0} = \left.\frac{\partial T}{\partial x}\right|_{x=X} = 0 \tag{5}$$

3.2 3D numerical model

A lattice of the domain in the three-dimensional model is shown in Fig. 4. The corresponding steady thermal transfer equation can be expressed as the following

$$\frac{\partial}{\partial x}(\lambda_{i,j,k}\frac{\partial T}{\partial x}) + \frac{\partial}{\partial y}(\lambda_{i,j,k}\frac{\partial T}{\partial y}) + \frac{\partial}{\partial z}(\lambda_{i,j,k}\frac{\partial T}{\partial z}) = 0 \tag{6}$$

where $\lambda_{i,j,k}$ is the thermal conductivity and T is the temperature. For the case of cubic voxels, the above equation can be discretized as follows

$$\begin{aligned}
&-(T(i+1, j,k) - T(i, j,k)) \cdot \lambda(i+1/2, j,k) \\
&+(T(i, j,k) - T(i-1, j,k)) \cdot \lambda(i-1/2, j,k) \\
&-(T(i, j+1,k) - T(i, j.,k)) \cdot \lambda(i, j+1/2,k) \\
&+(T(i, j,k) - T(i, j-1,k)) \cdot \lambda(i, j-1/2,k) \\
&-(T(i, j,k+1) - T(i, j,k)) \cdot \lambda(i, j,k+1/2) \\
&+(T(i, j,k) - T(i, j,k-1)) \cdot \lambda(i, j,k-1/2) = 0
\end{aligned} \tag{7}$$

where*λ(i+1/2,j,k)* also represents the thermal conductivity between lattices centers*(i,j,k)* and *(i+1,j,k)*. These terms can be expressed as follows

$$\lambda(i+1/2, j,k) = 2/(\frac{1}{\lambda(i, j,k)} + \frac{1}{\lambda(i+1, j,k)}) \tag{8}$$

The thermal conductivity *λ(i,j,k)* is assigned to the voxels in a similar way as for the pixels in the 2D model. In addition, a zero flux boundary condition is applied for the other four lateral faces. The corresponding mathematical expression of boundary condition can be expressed as the following

$$\begin{aligned}
&\left.\frac{\partial T}{\partial x}\right|_{x=0} = \left.\frac{\partial T}{\partial x}\right|_{x=X} = 0 \\
&\left.\frac{\partial T}{\partial z}\right|_{z=0} = \left.\frac{\partial T}{\partial z}\right|_{z=Z} = 0
\end{aligned} \tag{9}$$

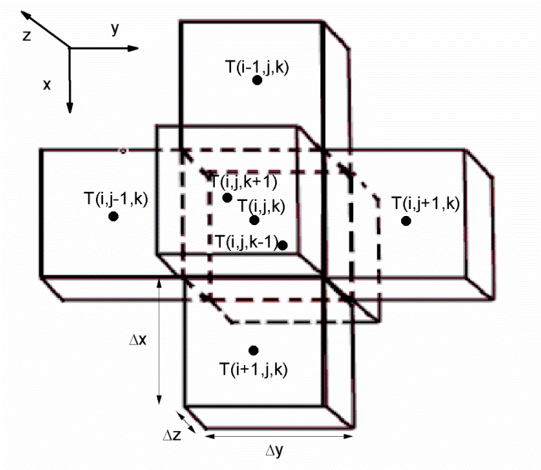

Fig. 4 Schematic view of a cell in the 3D model, including the six neighbors of the cell

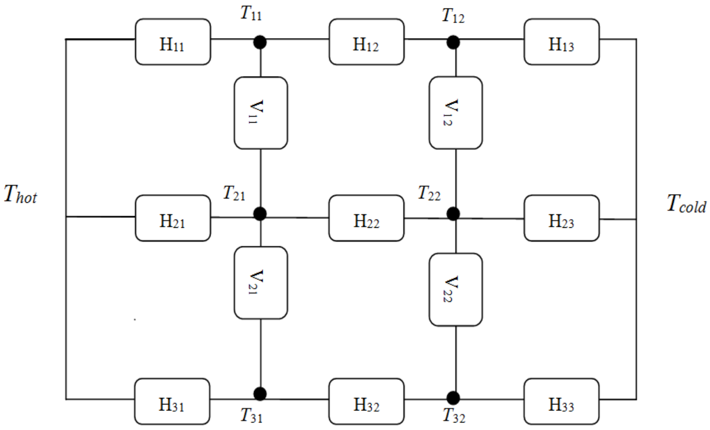

Fig. 5 Schematic overview of a 2D thermal resistor network (X×Y=3×4)

3.3 2D and 3D sparse matrix

Applying Eq. (3) and Eq. (7) to all cells in the 2D and 3D models, respectively, we will have P equations ($P_{2D}= X\times(Y-2), P_{3D}=X\times(Y-2)\times Z$) for P unknown cell temperatures. Both Eq. (3) and Eq. (7) can be written in a matrix form as follows

$$\tilde{\Gamma}\vec{T} = \vec{S} \tag{10}$$

where the matrix $\tilde{\Gamma}$ is a sparse multi-diagonal symmetrical matrix and $\vec{T}$ is a vector of P components which corresponds to the unknown cell temperatures. The vector $\vec{S}$ has a length P and is composed of zero values with the exception of the edge elements (y=0 and y=Y) in which the boundary temperatures are imposed (the temperatures of 273.5K and 313.5K, respectively).

As an illustration, Eq. (3) can be written for a 3×4 two-dimensional network (see Fig.5) as the following

$$\begin{pmatrix} D_{11} & V_{11} & 0 & H_{12} & 0 & 0 \\ V_{11} & D_{21} & V_{21} & 0 & H_{22} & 0 \\ 0 & V_{21} & D_{31} & 0 & 0 & H_{32} \\ H_{12} & 0 & 0 & D_{12} & V_{12} & 0 \\ 0 & H_{22} & 0 & V_{12} & D_{22} & V_{22} \\ 0 & 0 & H_{32} & 0 & V_{22} & D_{32} \end{pmatrix} \begin{pmatrix} T_{11} \\ T_{21} \\ T_{31} \\ T_{12} \\ T_{22} \\ T_{32} \end{pmatrix} = T_{hot} \begin{pmatrix} -H_{11} \\ -H_{21} \\ -H_{31} \\ 0 \\ 0 \\ 0 \end{pmatrix} + T_{cold} \begin{pmatrix} 0 \\ 0 \\ 0 \\ -H_{13} \\ -H_{23} \\ -H_{33} \end{pmatrix}$$

While for a 3×4×2 three-dimensional network (see Fig.6), Eq. (7) can be written as the following

$$\begin{pmatrix} D_{111} & V_{111} & 0 & H_{121} & 0 & 0 & B_{111} & 0 & 0 & 0 & 0 & 0 \\ V_{111} & D_{211} & V_{211} & 0 & H_{221} & 0 & 0 & B_{211} & 0 & 0 & 0 & 0 \\ 0 & V_{211} & D_{311} & 0 & 0 & H_{321} & 0 & 0 & B_{311} & 0 & 0 & 0 \\ H_{121} & 0 & 0 & D_{121} & V_{121} & 0 & 0 & 0 & 0 & B_{121} & 0 & 0 \\ 0 & H_{221} & 0 & V_{121} & D_{221} & V_{221} & 0 & 0 & 0 & 0 & B_{221} & 0 \\ 0 & 0 & H_{321} & 0 & V_{221} & D_{321} & 0 & 0 & 0 & 0 & 0 & B_{321} \\ B_{111} & 0 & 0 & 0 & 0 & 0 & D_{112} & V_{112} & 0 & H_{122} & 0 & 0 \\ 0 & B_{211} & 0 & 0 & 0 & 0 & V_{112} & D_{212} & V_{212} & 0 & H_{222} & 0 \\ 0 & 0 & B_{311} & 0 & 0 & 0 & 0 & V_{212} & D_{312} & 0 & 0 & H_{322} \\ 0 & 0 & 0 & B_{121} & 0 & 0 & H_{122} & 0 & 0 & D_{122} & V_{122} & 0 \\ 0 & 0 & 0 & 0 & B_{221} & 0 & 0 & H_{222} & 0 & 0 & D_{222} & V_{222} \\ 0 & 0 & 0 & 0 & 0 & B_{321} & 0 & 0 & H_{322} & 0 & V_{222} & D_{322} \end{pmatrix} \begin{pmatrix} T_{111} \\ T_{211} \\ T_{311} \\ T_{121} \\ T_{221} \\ T_{321} \\ T_{112} \\ T_{212} \\ T_{312} \\ T_{122} \\ T_{222} \\ T_{322} \end{pmatrix} = T_{hot} \begin{pmatrix} -H_{111} \\ -H_{211} \\ -H_{311} \\ 0 \\ 0 \\ 0 \\ -H_{112} \\ -H_{212} \\ -H_{312} \\ 0 \\ 0 \\ 0 \end{pmatrix} + T_{cold} \begin{pmatrix} 0 \\ 0 \\ 0 \\ -H_{131} \\ -H_{231} \\ -H_{331} \\ 0 \\ 0 \\ 0 \\ -H_{132} \\ -H_{232} \\ -H_{332} \end{pmatrix}$$

The off-diagonal elements *V*, *H* and *B* of matrix $\tilde{\Gamma}$ correspond to the thermal conductivity of the neighbor links in the *x*-direction, the*y*-direction, and in the thickness direction *z*, respectively. The diagonal elements, D, are the sum of the thermal conductivities of the neighbor links. Considering the case of a large system of equations, the use of iterative algorithms is required to accelerate the convergence and thus to reduce the required computational time. In a previous study (Wei *et al.* 2013), Eq. (10) was solved by using the Gauss-seidel iteration method. This method is simple, but the convergence of the method is relatively slow for large systems of equations. The solution to Eq. (10) for one statistical sample on a 60×60×20 system required approximately 2 hours of CPU time on a 2-GHz Intel PC with 4 GB of RAM. To overcome long computational times for large systems, the "Multi-frontal Massively Parallel Solver" package for solving linear systems of a square sparse matrix is used. MUMPS is a direct method based on a multi-frontal approach which performs a direct factorization (see http://mumps.enseeiht.fr/, and http://graal.ens-lyon.fr/MUMPS/). This method only requires the storage of non-zero elements. The solution for one statistical sample with the above-mentioned system requires no more than a few seconds on a 15-processor parallel computer.

Once the temperature distribution over the lattice is determined, the heat fluxes Q_k along the *y* direction that pass through each horizontal slice of the lattice (3D) can be calculated. These fluxes are equal for all the slices under steady-state conditions. Then, the effective thermal conductivity k_{eff} between the hot and cold slabs in the 3D model can be simply obtained by following

$$k_{eff} = \frac{Q_k \cdot Y}{X \cdot Z} \times \frac{1}{T_{hot} - T_{cold}} \tag{11}$$

Regarding the 2D model, the lattice number in the z direction is equal to 1, thus k_{eff} can be expressed as the following

$$k_{eff} = \frac{Q_k \cdot Y}{X} \times \frac{1}{T_{hot} - T_{cold}} \tag{12}$$

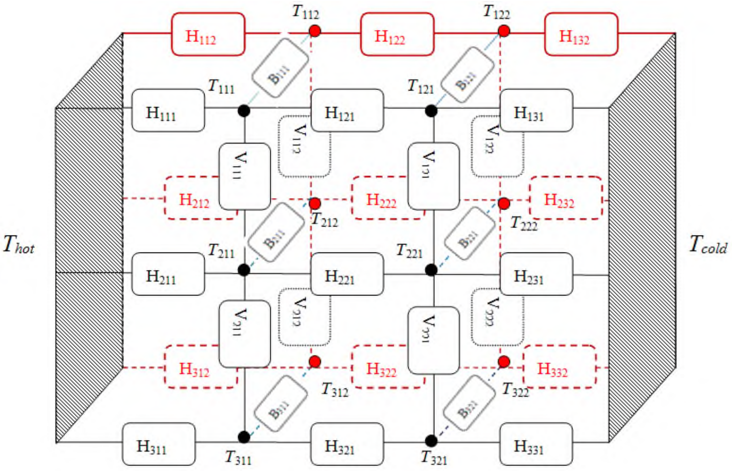

Fig. 6 Schematic overview of a 3D thermal resistor network (X×Y×Z=3×4×2)

4. Thermal conductivity of cement paste and pores

An experimental value of 0.5Wm^{-1}K^{-1}, determined for a fully dense sample (without the air agent), was used for the thermal conductivity of the solid phase. This value is consistent with other literature values (Mydin and Wang 2012, Fu and Chung 1999). To approximate the pores, they are assumed as approximation that they contain trapped air for which the thermal conductivity may be estimated as 0.025Wm^{-1}K^{-1} (Bouvard D *et al.* 2007) at room temperature. The thermal conductivity of air tends to increase with temperature; however, the Knudsen effect (Collishaw and Evans 1994, Litovsky *et al.* 1996) tends to decrease this thermal conductivity. Therefore, the influence of micro pores in cement paste on the thermal conductivity of air was not considered in the present study.

5. Pore structure characterization and the 2D and 3D reconstructed structure

5.1 Pore structure characterization by XCT

By using three-dimensional X-ray computerized tomography (XCT) coupled with 3D image processing technology, the porosity and pore size distribution within the porous material can be easily detected because of the high degree of contrast between the X-ray attenuation coefficient of the pores and the cement paste matrix.

In this study, all samples were visually examined with Y.CT Precision System (YXLON, Germany).The detector type is flat panel Y.XRD1620. Because of the relatively low density of this type of concrete, a 80 kV X-ray tube potential was used with a corresponding resolution of 10μm/pixel. An example of a 3D image is presented in Fig.7. Different colors denote different levels of pore sizes in the three dimensional space. As shown in Fig.8, the size distribution of pores in a typical cellular concrete (non-AAC) follows a log-normal distribution. A probability density function, denoted by $f_x(x; \mu, \sigma)$, was used to fit the size distribution

$$f_x(x;\mu,\sigma) = \frac{1}{x\sigma\sqrt{2\pi}} e^{-\frac{(\ln x-\mu)^2}{2\sigma^2}}, x > 0 \tag{13}$$

where μ and σ are the mean and standard deviation of the logarithm of the variable, respectively. In this study, the fitted parameters are μ=4.65 and σ= 0.395. The value of the goodness of fit is 0.985. Regarding the porosity, six 3D-images were analyzed, and the results were then averaged. Therefore, the computed total porosity is 67.2% ±1.2%,

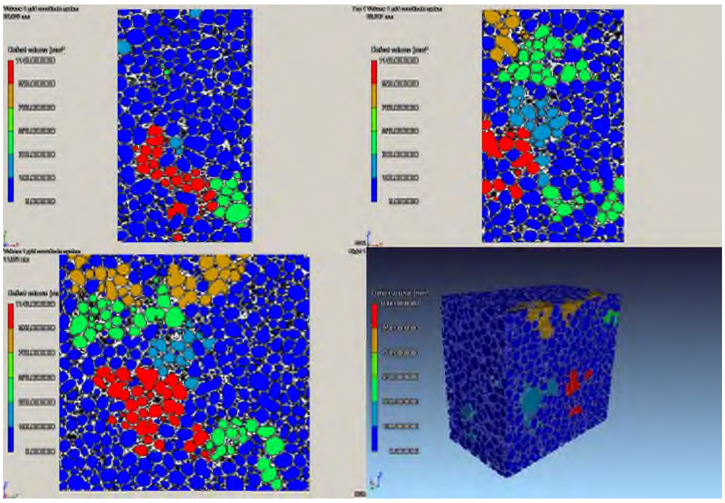

Fig. 7 Extraction and 3D-visualization of pore structures from a non-autoclaved aerated concrete

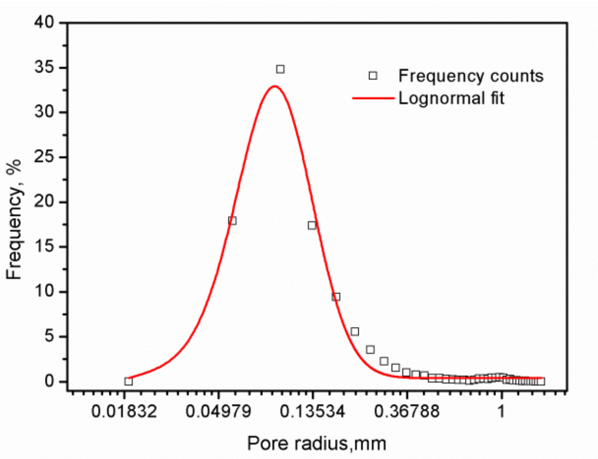

Fig. 8 Pore size distribution of non-AAC. The fitted parameters are μ=4.65, and σ= 0.395. R^2=0.985

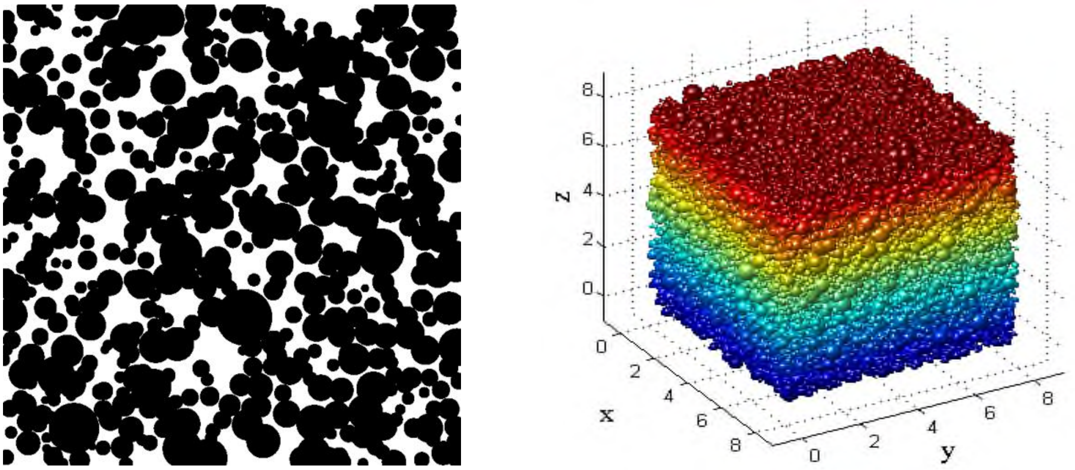

(a) 2D reconstructed image (b) 3D reconstructed image

Fig. 9 2D and 3D reconstructed images

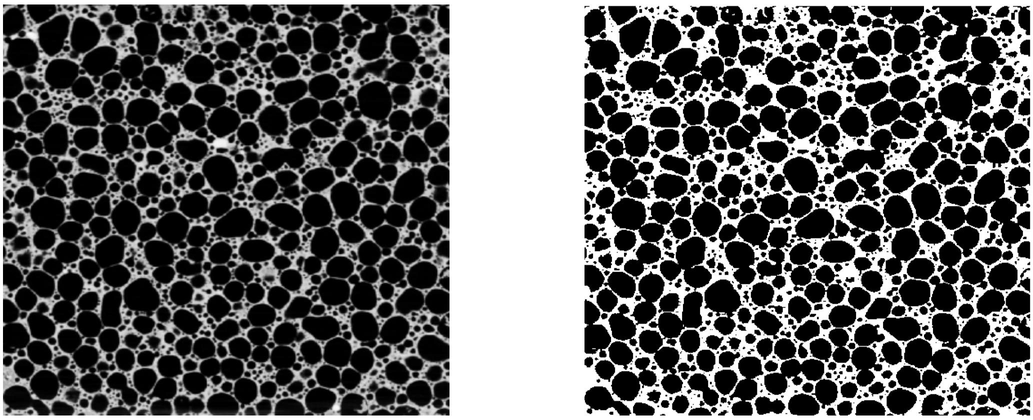

(a) Original image (b) binary image

Fig. 10a 2D real porous structure from the 3D cross-sectional XCT image (a) Original image, (b) binary image

5.2 Generation of 2D and 3D artificial pore structure

Similar to the method presented by Wei She (Wei *et al*. 2013), the porous structure of a non-AAC was determined through a random generation method and represented by an artificial image consisting of two phases: the pores and the cement paste matrix. In the 2D model, the pores were described as circles (spheres in the 3D model) and in stochastic spatial distributions in the solid matrix with the following regulation rules:

(1) Each pore radius follows the log-normal distribution function as mentioned above with a mean value, μ, and a standard deviation parameter, σ. In this paper, the pore diameters were selected to bein the range of $\mu \pm 3\sigma$to produce a more realistic structure.

(2) All generated pores are permitted to be invaded, but the overlap area ratio (overlap volume ratio in the 3D model), δ, should be no more than a set value ($\delta \leq 0.4$).

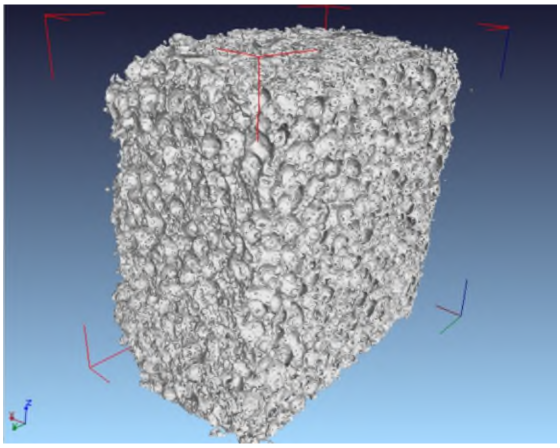

Fig. 10b Illustration of the 3D morphology of cellular concrete

(3) The target pores are searched until the porosity attains the given value.
With these settings and parameters, the reconstructed 2D and 3D porous structures (see Fig. 9), containing 500×500 pixels and 80×80×80 voxels, respectively, were constructed considering the following calculation.

5.3 Application of the FVM to the tomographic image

The FVM presented in Section 3 was also applied to the real 2D and 3D porous structures obtained from X-ray tomographic images of cellular concrete. These images are in voluminous files containing the gray levels of the voxels that forms a cubic piece of the foam sample. The resolution used, which corresponds to the voxel size, was approximately 10µm.Thresholding and filtering operations were first applied to obtain a binary repartition of the voxels in the solid or gas phase. The image obtained must have a gas volume fraction corresponding to the porosity of the cellular concrete analyzed. Fig. 10(a) shows a slice of a tomographic image from a 3Dtomographic image (Fig. 10(b)) of cellular concrete before and after the thresholding and filtering process. At the end of these operations, a binary matrix of the cubic voxels and their state (1: solid; 0: gas) was obtained. The finite volume numerical calculation was then applied to this discretization.

6. Numerical results and analysis

6.1 Benchmarks

To validate the algorithm and the codes of the 2D and 3D models, the numerical predictions are compared with the theoretical solutions for two hypothetical structural cases: parallel mode and series mode (see Table 1).The porous structures are formed in two phases, and the thermal conductivities are 0.5Wm^{-1}K^{-1} ()and 0.025Wm^{-1}K^{-1}. To simplify the comparison, the fractions of the two phases are equal. Therefore, the calculated effective thermal conductivity is 0.2625Wm^{-1}K^{-1} for the parallel mode and 0.04762Wm^{-1}K^{-1} for the series mode. Table 1 lists our predictions of the ETCs and the deviations from the simple analytical solutions as functions of the lattice number.

Table1 Predictions of effective thermal conductivities for two types of structures (parallel and series modes)

Lattice number (X× Y× Z)		Parallel mode		Series mode	
		Predictions, $Wm^{-1}K^{-1}$	Deviations,%	Predictions, $Wm^{-1}K^{-1}$	Deviations,%
2D	10× 10	0.2917	11.12	0.0529	11.09
	60 × 60	0.2669	1.68	0.0484	1.64
	80× 80	0.2658	1.26	0.0482	1.21
3D	10× 10 × 10	0.2917	11.12	0.0529	11.09
	60× 60 × 60	0.2669	1.68	0.0484	1.64
	80× 80 × 80	0.2658	1.26	0.0482	1.21

Notably, the predicted values by the 2D model are identical to the corresponding 3D model. The reason for this is that the 3D structures of the parallel mode and series mode are repetitive or symmetrical in the thickness direction (z).

It is also clear that our predictions agree with the theoretical solutions with a maximum deviation of less than 2% when the lattice number is larger than 60. The results validate the proposed algorithm and processing boundary conditions. Larger lattice number results in more accurate modeling results. However, these larger lattices require a higher computational cost. In the following modeling, the lattice number was set to 80× 80× 80 for the 3D model and 500× 500 for the 2D model unless specified.

6.2 Computation of the thermal conductivity for the 2D and 3D models

The thermal conductivity corresponding to each image was predicted by both 2D and 3D modeling. To obtain a reliable value, 6 cross-sections (500×500 pixels) of the 3D-XCT image were used and the results were then averaged. Examples of the numerical modeling of the temperature distribution of the2D and 3D reconstructed structures are shown in Fig. 11. Similar results can also be found from the numerical modeling performed on the 2D and 3D real structures. The typical run times for the longer simulations discussed in this paper require 20 minutes on a 3GHz Core (2) PC having 4GB of memory.

Because these results were derived from a real image, the 2D reconstructed image was evaluated against the calculated thermal conductivity from the corresponding real 2D images. The calculated results showed that the 2D thermal conductivities were 0.123±0.01 $Wm^{-1}K^{-1}$ for the reconstructed 2D image and, 0.121±0.04 $Wm^{-1}K^{-1}$ for the real cross-sectional 2D images (shown in Table 2). These close results highlighted that the 2D reconstructed image presented nearly the identical characteristics as the real cellular concrete in terms of computed cross-sectional thermal conductivity.

Additionally, 3D calculations were performed for the 3D real and reconstructed images. The corresponding predicted thermal conductivities were nearly identical (0.153 $Wm^{-1}K^{-1}$ and 0.154 $Wm^{-1}K^{-1}$, shown in Table 2), and both 3D predictions were found to be in better agreement with the experimental result (0.158$Wm^{-1}K^{-1}$) than the 2D modeling results. This consistent result indicates that the 3D reconstructed image generated in this paper can represent a real non-AAC in terms of thermal conductivity. Additionally, the 3D calculated thermal conductivity is higher than the 2D calculated thermal conductivity by approximately 25% for the identical image generation parameters.

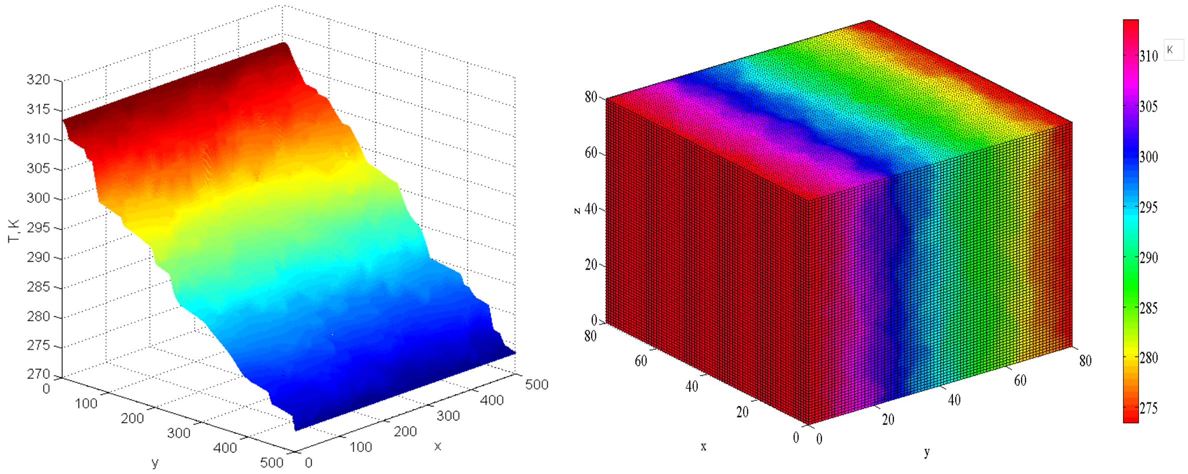

(a) 2D reconstructed structure (b) 3D reconstructed structure

Fig. 11 Numerical calculated temperature distribution of the 2D and 3D reconstructed structure

Table 2 Predicted thermal conductivities calculated based on different types of images with 2D and 3D modeling, using a FVM

Structure type	#Porosity (%)	Models	Thermal conductivity, $Wm^{-1}K^{-1}$	
			FVM	Measured
Real pore structure	67.25	2D	0.121±0.04	0.158
X-CT	67	3D	0.153	
Reconstructed image	67.2	2D	0.123±0.01	-
	67.22	3D	0.154	-
Dense material	0	-	-	0.5

*The conditions for the production of non-autoclaved aerated concrete and characterization of the thermal conductivity are described in previous studies [34-36].

6.3 Comparison between 2D and 3D modeling

Using the model or real sectional image from 3D-XCT image, the 2D calculated thermal conductivities are lower than the 3D conductivities (Table 2). This disparity was additionally checked in different 3D structures of a different type of non-AAC (foamed concrete). The porosity of this non-AAC varied at 12%, 21.39%, 35.5%, 47.24%, 59% 75.45% 79.19% and 84.17%, and the corresponding input parameters and pore size distribution are taken from previous study (Wei *et al.* 2013). The computations were implemented for all of the above images, and the results are shown in Fig. 12.

From Fig. 12, the 3D computed thermal conductivity is higher than the 2D conductivity. In the 2D model, each pixel exchanges heat with the neighboring pixels in the plane. Therefore, the heat flow that is perpendicular to the section is not considered. In principle, this assumption is only applicable if the microstructure in the third dimension is repetitive or symmetrical (as discussed in section 6.1). However, this assumption is not representative for real cellular concrete. The 3D model better captures the real situation that occurs in disordered materials such as aerated concretes. In the third direction, a new path is supplied for heat transfer around the pores. Therefore, the thermal obstructive action of pores is weakened, compared with the 2D case. For

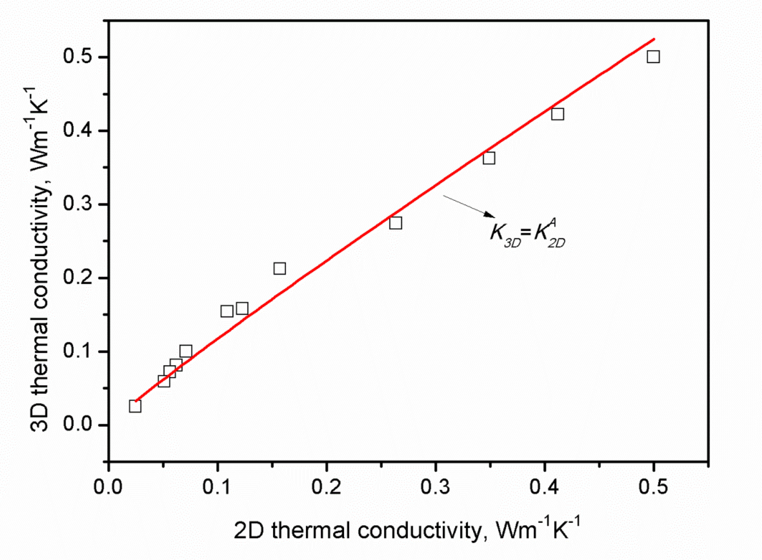

Fig. 12 Relationship between the 2D and 3D computed thermal conductivities for non-AACs with different porosities. The fitted parameters are A = 0.9307, with a R^2=0.9862.

this reason, the 3D computed thermal conductivity is higher than the2D values. Thus, the use of 3D modeling is strongly recommended for aerated concretes and the results are expected to be closer to experimental values.

It was also found that a power law function could rather accurately define the relationship between the 2D and 3D results (the red curve shown in Fig. 12). This relationship can be expressed as follows

$$k_{3D} = k_{2D}^{A} \tag{14}$$

where A is equal to 0.9307and the goodness of fit, R^2 is equal to 0.9862. Therefore, the 3D numerical results can be predicted from the 2D value through equation 14. Additionally, this empirical equation improves the application of the 2D image-based modeling, because the 2D images of aerated concretes can be more readily obtained (e.g., SEM, microscope, or even a high pixel camera) and easily digitalized in common software (e.g., Matlab and Image-Pro). However, obtaining the 3D microstructure parameters from 3D-XCT is relatively difficult, expensive, and time consuming. By using the function between the 2D and 3D numerical predictions, 2D image-based analyses (instead of 3D image-based analyses) could remain an alternative reliable method for predicting the effective thermal conductivity.

7. Conclusions

The present work implemented 2D and 3D image-based finite volume models to analyze the heat transfer properties in porous structures, such as non-aerated concrete. The 2D and 3D reconstructed matrix-pore structures were generated based on the collective microstructural information obtained by 3D-XCT images of non-aerated concrete. The real and reconstructed images (2D and 3D) were then evaluated by computing the corresponding effective thermal conductivity. The predicted effective thermal conductivity obtained by 2D computations performed on 2D reconstructed structures agreed with the values derived for cross-sections of the real 3D-XCT image (0.121Wm^{-1} K^{-1} for the real cross-sections and 0.123 Wm^{-1}K^{-1} for the artificial 2D image). The 3Dcalculated thermal conductivity values determined from real 3D and reconstructed structures were nearly identical (0.153Wm^{-1} K^{-1} for the real 3D-XCT imageand0.154Wm^{-1}K^{-1} for the artificial 3D image). The predictions from the 3D analysis were higher than the 2D predictions. However, the 3D predictions better agree with the experimental value of 0.158 Wm^{-1} K^{-1}.

The reason for the differences between the 3D and 2D predictions is that the heat conduction in the third dimension is omitted in the2D simulation. This omission produces an underestimation of the effective thermal conductivity for identical boundary conditions. A power law function fitted the relationship between the 2D and 3D calculated data. This function was confirmed for another type of non-AAC (foamed concretes) with different porosities (12%-84.17%) and different pore size distributions. Therefore, this relationship is expected to be valid for all non-AACs, allowing the use of this easier to implement 2D image-based model.

Acknowledgements

The authors would like to appreciate for the financial support by National Natural Science Fund of China (5150080804), 973 Program (2015CB655100) and Technological Development Projects of China Railway Engineering Corporation (Z2013-038, 2013G001-A, 2015G002-I, 2015G002-K).

References

Ahern, A., Verbist, G., Weaire, D., Phelan, R. and Fleurent, H. (2005), “The conductivity of foams: a generalisation of the electrical to the thermal case”, *Colloid Surface A*: *Physicochem. Eng. Aspects*, **263**, 275-279.

Aldridge, D. (2000), “Foamed concrete for highway bridge works, Seminar notes on foamed concrete: properties, applications and potential”, University of Dundee, Scotland, 33-41.

Bhattacharya, A., Calmidi, V. and Mahajan, R. (2002), “Thermophysical properties of high porosity metal foams”, *Int. J. Heat Mass Transfer*, **45**(5), 1017-1031.

Bouvard, D., Chaix, J.M., Dendievel, R., Fazekas, A., Létang, J.M., Peix, G. and Quenard, D. (2007), “Characterization and simulation of microstructure and properties of EPS lightweight concrete”, *Cement and Concrete Res.*, **37**(12), 1666-1673.

Collishaw, P.G. and Evans, J.R.G. (1994), “An assessment of expressions for the apparent thermal conductivity of cellular materials”, *J. Mater. Sci.*, **29**(9), 2261-2273.

EN 12664 (2001), *Thermal performance of building materials and products -determination of thermal resistance by means of guarded hot plate and heat flow meter methods-dry and moist products of medium and low thermal resistance*, European Committee for Standardization.

EN 12939 (2000), *Thermal performance of building materials and products -determination of thermal resistance by means of guarded hot plate and heat flow meter methods -thick products of high and medium thermal resistance*, European Committee for Standardization.

Esmaily, H. and Nuranian, H. (2012), “Non-autoclaved high strength cellular concrete from alkali activated slag”, *Constr. Build. Mater.*, **26**(1), 200-206.

Fu, X. and Chung, D. (1999), "Effect of admixtures on thermal and thermomechanical behavior of cement paste", *ACI Mater. J.*, **96**(4), 455-61.

Gibson, L.J. and Ashby, M.F. (1997), *Cellular Solids*, (second ed.), Cambridge University Press, Cambridge, UK.

Glicksmann, L.R. and Schuetz, M.A. (1994), *Low density cellular plastics*, Chapman & Hall, London, UK.

Hashin, Z. and Shtrikman, S. (1962), "A variational approach to the theory of the effective magnetic permeability of multiphase materials", *J. Appl. Phys.*, **33**(10), 3125-3131.

ISO 8990 (1994), *Thermal insulation-determination of steady-state thermal transmission properties-calibrated and guarded hot box*, International Standard Organization.

Jones, M.R. and McCarthy, A. (2005), "Behavior and assessment of foamed concrete for fill and highway applications", *Proceedings of an International Conference on Uses of Foamed Concrete Global Construction: Ultimate Concrete Opportunities*, Dundee, Scotland, UK.

Kearsley, E.P. and Mostert, H.F. (2005), "Opportunities for expanding the use of foamed concrete in the construction industry", *Proceedings of an International Conference on Uses of Foamed Concrete Global Construction: Ultimate Concrete Opportunities*, Dundee, Scotland, UK.

Kuhn, J., Ebert, H., Arduini-Schuster, M.C., Büttner, D. and Fricke, J. (1992), "Thermal transport in polystyrene and polyurethane foam insulations", *Int. J. Heat Mass Transfer*, **35**(7), 1795-1801.

Landauer, R. (1952), "The electrical resistance of binary metallic mixtures", *J. Appl. Phys.*, **23**(7), 779-784.

Litovsky, E., Shapiro, M. and Shavit, A. (1996), "Gas pressure and temperature dependences of thermal conductivity of porous ceramic materials: Part 2, refractories and ceramics with porosity exceeding 30%", *J. Am. Ceramic Soc.*, **79**(5), 1366-1376.

Lu, T.J. and Chen, C. (1999), "Thermal transport and fire retardance properties of cellular aluminium alloys", *Acta Mater.*, **47**(5), 1469-1485.

Lv, X., Cao, M., Li, Y., Li, X., Li, Q., Tang, R., Wang, Q. and Duan, Y. (2015), "A new absorbing foam concrete: preparation and microwave absorbing properties", *Adv. Concrete Constr.*, **3**(2),103-111.

Narayanan, N. and Ramamurthy, K. (2000) "Structure and properties of aerated concrete: a review", *Cement Concrete Compos.*, **22**(5), 321-329

Nooraini, M.Z., Ismail, A.R. and Ahmad Mujahid, A.Z. (2009), "Foamed concrete: potential application in thermal insulation, Malaysian Technical Universities Conference on Engineering and Technology (MUCEET), Kuantan, Pahang, Malaysian, June.

Othuman Mydin, M.A. and Wang, Y.C. (2012), "Thermal and mechanical properties of lightweight foamed concrete at elevated temperatures", *Mag. Concrete Res.*, **64**(3), 213-224.

Placido, E., Arduini-Schuster, M.C. and Kuhn, J. (2005), "Thermal properties predictive model for insulating foams", *Infrared Phys. Techn.*, **46**(3), 219-231.

Russell, H.W. (1935), "Principles of heat flow in porous insulators", *J. Am. Ceram. Soc.*, **18**(1-12), 1-5.

Scheffler, M. and Paolo, C. (2005), *Cellular ceramics structure, manufacturing, properties and applications*, WILEY-VCH, Weinheim, Germany.

She, W., Chen, Y., Zhang, Y. and Jones, M.R. (2013), "Characterization and simulation of microstructure and thermal properties of foamed concrete", *Constr. Build. Mater.*, **47**, 1278-1291.

Skochdopole, R.E. (1961), "The thermal conductivity of foam plastics", *Eng. Progress*, **57**.

Tanaçan, L., Ersoy, H.Y. and Arpacıoğlu, Ü. (2009), "Effect of high temperature and cooling conditions on aerated concrete properties", *Constr. Build. Mater.*, **23**(3), 1240-1248.

Wang, X.S., Wu, B.S. and Wang, Q.Y. (2005), "Online SEM investigation of microcrack characteristics of concretes at various temperatures", *Cement Concrete Res.*, **35**(7), 1385-1390.

Wiener, O. (1904), "Lamellare doppelbrechung", *Phys. Zeitschrift*, **5**(12), 332-338.

Xia, Y., Yan, Y. and Hu, Z. (2013), "Utilization of circulating fluidized bed fly ash in preparingnon-autoclaved aerated concrete production", *Constr. Build. Mater.*, **47**, 1461-1467.

Yang, L., Yan, Y. and Hu, Z. (2013), "Utilization of phosphogypsum for the preparation of non-autoclaved aerated concrete", *Constr. Build. Mater.*, **44**, 600-606.

Yesilata, B. and Turgut, P. (2007), "A simple dynamic measurement technique for comparing thermal insulation performances of anisotropic building materials", *Ener. Build.*, **39**(9), 1027-34.

Zarr, R.R. (2001), “History of testing heat insulators at the national institute of standards and technology”, *ASHRAE Transact.*, **107**(2), 1-11.

CC